

Separability of drag and thrust in undulatory animals and machines

Rahul Bale,^{1,+} Anup A. Shirgaonkar,^{1,+} Izaak D. Neveln,² Amneet Pal Singh Bhalla,¹
Malcolm A. MacIver,^{1,2,3,*} and Neelesh A. Patankar^{1,*}

1 Department of Mechanical Engineering, Northwestern University,

2 Department of Biomedical Engineering, Northwestern University,

3 Department of Neurobiology, Northwestern University,

2145 Sheridan Road, Evanston, IL 60208, USA

+ Authors made equal contributions

*** Authors for correspondence (n-patankar@northwestern.edu, maciver@northwestern.edu)**

Abstract

For nearly a century, researchers have tried to understand the swimming of aquatic animals in terms of a balance between the forward thrust from swimming movements and drag on the body. Prior approaches have failed to provide a separation of these two forces for undulatory swimmers such as lamprey and eels, where most parts of the body are simultaneously generating drag and thrust. We nonetheless show that this separation is possible, and delineate its fundamental basis in undulatory swimmers. Our approach unifies a vast diversity of undulatory aquatic animals (anguilliform, sub-carangiform, gymnotiform, balistiform, rajiform) and provides design principles for highly agile bioinspired underwater vehicles. This approach has practical utility within biology as well as engineering. It is a predictive tool for use in understanding the role of the mechanics of movement in the evolutionary emergence of morphological features relating to locomotion. For example, we demonstrate that the drag-thrust separation framework helps to predict the observed height of the ribbon fin of electric knifefish, a diverse group of neotropical fishes which are an important model system in sensory neurobiology. We also show how drag-thrust separation leads to models that can predict the swimming velocity of an organism or a robotic vehicle.

1 Introduction

The hydrodynamics of aquatic locomotion has importance across multiple domains, from basic biology to the engineering of highly maneuverable underwater vehicles. Within biology, beyond the interest in aquatic locomotion, there is extensive use of several aquatic model systems within neuroscience such as lamprey for research into spinal cord function [1], zebrafish for developmental neuroscience [2], and weakly electric fish for the neurobiology of sensory processing (reviews: [3, 4]). Within engineering, the maneuverability and efficiency of fish is inspiring new styles of propulsion and maneuvering in underwater vehicles [5–7]. The implementation of engineered solutions will depend on the resolution of open issues in hydrodynamics of aquatic locomotion. Finally, an understanding of the hydrodynamics of aquatic locomotion is critical for insight into the evolution of fish [8] and their land-based descendants.

While the hydrodynamics of swimming organisms have been studied actively for almost a century, there are key questions that remain unresolved. This work focuses on one such unresolved issue that pertains to the mechanisms of drag and thrust generation. The decomposition of the total force on a swimming organism into drag and thrust is desirable because it can fundamentally reveal how an organism produces forward push to balance the resistance to motion from the surrounding fluid. It can also lead to simple quantitative models to predict swimming velocity of organisms or artificial underwater vehicles based on their kinematics.

If we consider a boat with a propeller, the decomposition of thrust and drag is straightforward since all the thrust is coming from the propeller, and most of the drag is coming from the hull. However, in the case of anguilliform swimmers such as eels, where the entire body undulates, there are no distinct portions of the body that alone produce thrust or cause drag. In other groups of fishes there are undulatory elongated fins along the ventral midline (Fig. 1a, knifefish such as those of the Gymnotiformes and Notopteridae), dorsal midline (*Gymarchus nilotica*, the oarfish *Regalecus glesne*), along ventral and dorsal midlines (triggerfish of the Balastidae), and along the lateral margins of the body (certain rays and skates of the Batoidea, cuttlefish). For these animals, undulating fins may be regarded as the primary thrust generators and the relatively straight body may be regarded as the primary source of drag. However, this apparent decomposition of drag and thrust regions should not be considered to imply that an undulatory fin itself has no drag. This is clearly not the case because a hypothetical undulatory ribbon fin that is not attached to a body will undergo steady swimming. The drag of the ribbon fin and the thrust it generates

will be in balance in that case.

Arguably the most widely cited analysis of drag-thrust decomposition is due to Lighthill [10]. He considered the force generated from undulatory motion by elongated animals such as eels [11], and later, with Blake, considered forces on ribbon fins of balistiform and gymnotiform swimmers [12]. The analysis was based on a “reactive” theory of propulsion that was proposed for high Reynolds number swimming. Lighthill considered a decomposition of the force on the body into resistive and reactive components that lead to drag and thrust, respectively. He defined the force on a section of the body as resistive if it depends, linearly or non-linearly, on the instantaneous velocity of that section relative to the surrounding fluid. Reactive forces were defined as those due to inertia of the surrounding fluid (the “added mass” effect), proportional to the rate of change of the relative velocity between the fluid and surface of the swimming body. Lighthill then provided expressions for the reactive thrust force using a simplified potential flow theory [11,12]. No model for drag was developed.

To address this long standing issue, we define three fundamental principles for the decomposition of forces arising from undulatory swimming into drag and thrust. First, (D1) the body movement (kinematics) creating drag needs to be separated from the body movement creating thrust, such that the sum of these two movements results in the originally observed swimming motion of the animal. Second, (D2) these decomposed movements should be such that the surface of the body will move in a continuous fashion so that the kinematics can be realized in experiments or simulations. Third, (D3) the sum of the force due to the drag-inducing movement with the force due to the thrust-inducing movement needs to equal the force estimated from the original (undecomposed) movement of the fish. Requirement (D2) will enable three independent experiments to estimate forces and develop predictive models for swimming: i) the force based on the undecomposed motion; ii) the force resulting purely from the drag kinematics, defined as drag; iii) the force resulting purely from the thrust kinematics, defined as thrust.

In this work we propose a new way to decompose drag and thrust that satisfies conditions D1 to D3. Using an idealized elongated anal fin (hereafter ribbon fin) of weakly electric fish (Fig. 1a) but with no body as a model system, we present results from simulations and experiments supporting our approach. The scope of applicability of the decomposition will be further demonstrated through simulations of the eel *Anguilla rostrata*, the larval zebrafish *Danio rerio*, the black ghost knifefish *Apteronotus albifrons*, and the mackerel *Scomber scombrus*. These examples show where the decomposition is valid, and where it becomes invalid. For a case where it is valid—swimming with elongated fins such as in the knifefish—we

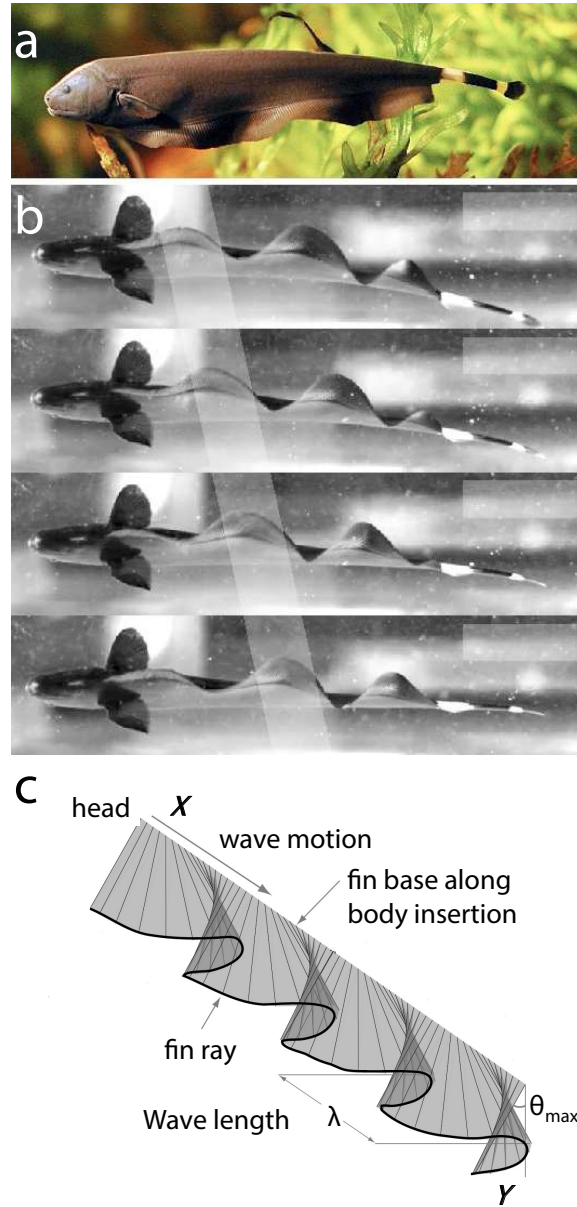


Figure 1. a) A median fin (ribbon fin) undulatory swimmer (gymnotiform swimmer): *Apteronotus albifrons*, the black ghost knifefish of South America (photograph courtesy of Per Erik Sviland). b) A backward traveling wave on the ribbon fin. c) Geometric configuration of the ribbon fin without the body for computations. Figure adapted from Fig. 1 of [9].

go on to show that drag thrust decomposition can be used to predict an important morphological feature: the height of the fin that maximizes cost of transport. Our predictions agree well with the measured height of the fin in a sample of 13 species in a representative family of knifefishes, the Aptereronotidae.

2 Results

2.1 Kinematic decomposition

To demonstrate drag–thrust decomposition, we consider the same model problem considered by Lighthill and Blake [12] and analyze the forces on the elongated median fin (hereafter “ribbon fin”) of a gymnotiform swimmer (Fig. 1a). We numerically simulate a translating ribbon fin with a traveling wave (Fig. 1b) along it. The traveling wave on the ribbon fin was described by the angular position of any point on the ribbon fin $\theta(x, t) = \theta_{\max} \sin 2\pi(\frac{x}{\lambda} - ft)$, where θ_{\max} is the maximum angle of excursion, f is the frequency, and λ is the wavelength of undulations. In the simulations there is no attached body. The fin morphology is shown in Fig. 1c. The force on the ribbon fin from the fluid is numerically computed for different values of the translational velocity U of the fin and the traveling wave velocity U_w (given by $f\lambda$). The wave motion is caused by the lateral oscillatory velocity field V_w on the fin surface. V_w , and by consequence U_w , were varied by changing the frequency f of the traveling wave. The fin had two waves along its length [9, 13].

To understand our proposed kinematic decomposition, consider a generic waveform of constant amplitude that has a lateral oscillatory velocity V_w and a corresponding traveling wave velocity U_w (Fig. 2-a1 & a2). Let U be the forward velocity of the fin as a whole. This is the undecomposed kinematics which is decomposed into two parts (Fig. 2-a2 & a3). The first decomposed motion, which we term the drag–causing *perfect slithering* motion, occurs when the forward velocity of the fin is equal to the backward velocity of the traveling wave (U_w). As a result, the fin appears to move along a stationary wave–shaped track (Fig. 2-b2). Each point on the fin has a velocity that is tangential to its surface (V_D in Fig. 2-a2). In this case the fluid is dragged forward by the tangential velocity along the fin surface which results in a backward (drag) force on the fin from the fluid. The second decomposed motion, which we term the thrust generating *frozen fin* motion, occurs when the fin is frozen in its undulatory shape, and that frozen shape drifts backward with a velocity equal to the velocity of the traveling wave minus the translational velocity of the fin ($U_w - U$), when U_w is greater than U . This motion pushes the fluid backward which

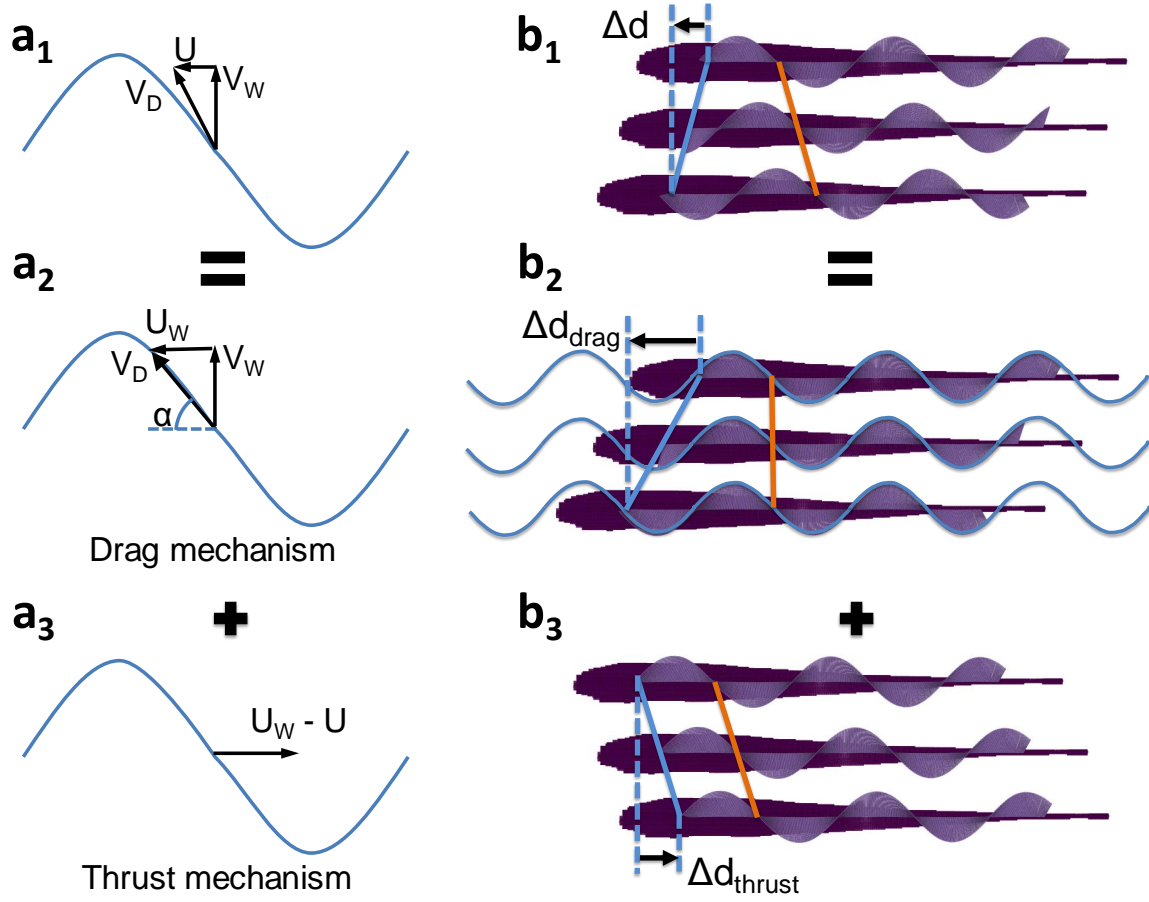


Figure 2. a) The proposed kinematic decomposition into drag and thrust producing mechanisms. The front end is on the left. b) The kinematic decomposition applied to a modeled black ghost knifefish. Each row, from top to bottom in each of the undecomposed, drag, and thrust mechanism, is at increasing instants of time.

in turn produces a forward (thrust) force on the fin (Fig. 2-a3 & b3).

In the idealization of the traveling wave as a sinusoid of constant amplitude, superposition of the kinematics of the perfect slithering and frozen fin motions results in the undecomposed kinematics of the fin surface. This fulfills both condition D1 (separated body movements add up to give original body movements) and condition D2 (the separated body movements are without discontinuities and physically realizable). This kinematic decomposition would be exact in case of an infinitely long fin. However, this is not the case for the finite fin length that we consider. For example, in the frozen fin case, the wave can be considered frozen in different phases. Despite this, our computational fluid simulations show that the thrust force does not depend strongly on the phase as long as there is more than one full wave on the fin, as is the case here. We next show that the kinematic decomposition also fulfills the requirement that the force of drag and the force of thrust sum to the undecomposed force from the fin (D3).

2.2 Dynamic decomposition

Dynamic decomposition here implies the decomposition of forces on the swimming body. Without loss of generality we consider a traveling wave that is moving backward, as in Fig. 1b. If the decomposition into drag and thrust is valid, then the total force F on the fin should satisfy the following equation

$$F[U, U_w] = \text{sgn}[U_w - U] T[U_w - U] - D[U_w], \quad (1)$$

where square brackets indicate “function-of”, T is thrust, D is drag, and $\text{sgn}[\cdot]$ gives the sign of the argument. The data for $F[U, U_w]$ are plotted in Fig. 3a.

We performed a separate set of simulations for the perfect slithering motion ($U = U_w$) for different values of U_w . The force on the ribbon-fin in this case is $D[U_w]$, which is plotted in Fig. 3b.

Using Eqn. 1 and the results in Fig. 3b we calculate the thrust $T[U_w - U]$ for each data point in Fig. 3a. If the decomposition is valid then the resulting data should be a well defined function of $U_w - U$. This is found to be so in Fig. 3c. Additionally, the results for $T[U_w - U]$, obtained above, should also match results from another set of simulations for the frozen fin case. To check this we performed frozen fin simulations for different values of the fin translational velocity U_f . There is no traveling wave in this case. The force on the ribbon fin in this case is $T[U_f]$ which should be the same function as $T[U_w - U]$ with U_f replaced by $(U_w - U)$. The solid line of Fig. 3c confirms this expectation.

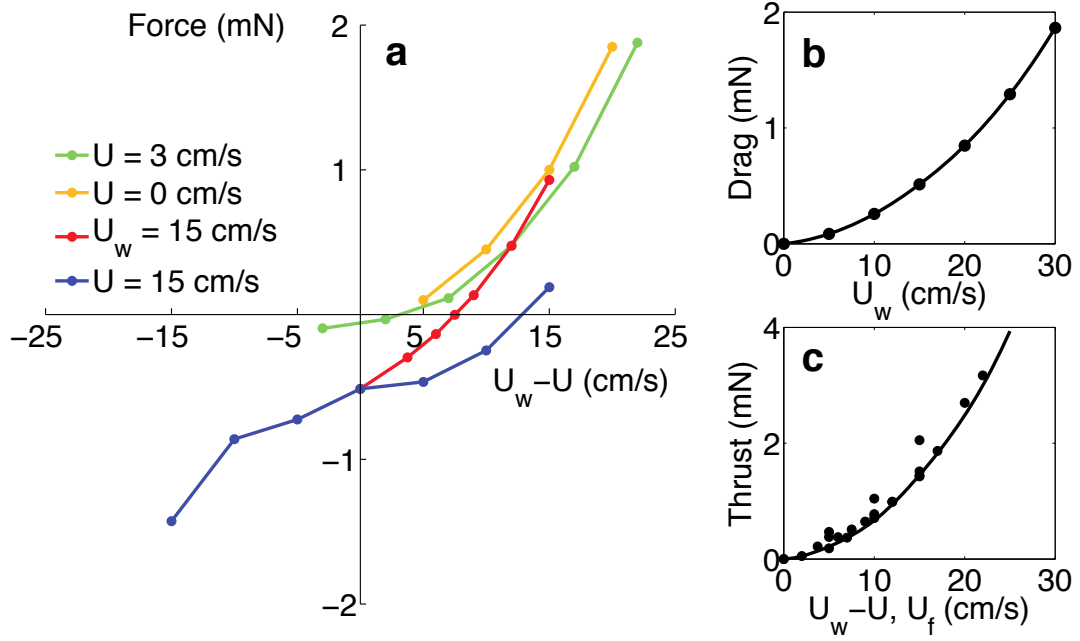


Figure 3. a) The computed total force on the ribbon fin vs. $U_w - U$ for different parameters. The legend identifies different simulation sets. For example, the set with $U_w = 15$ cm/s was the one where U_w was fixed and the value of U was changed. b) Drag, i.e., the force on a ribbon fin during perfect slithering motion. c) Thrust T computed as a function of $U_w - U$ for each data point in (a) by assuming the kinematic decomposition (Fig. 2 and Eqn. 1). These data are shown by solid dots. Separate frozen fin simulations were conducted as a function of U_f , shown by the dashed line. The dots cluster along this line giving evidence for the successful decomposition of drag and thrust.

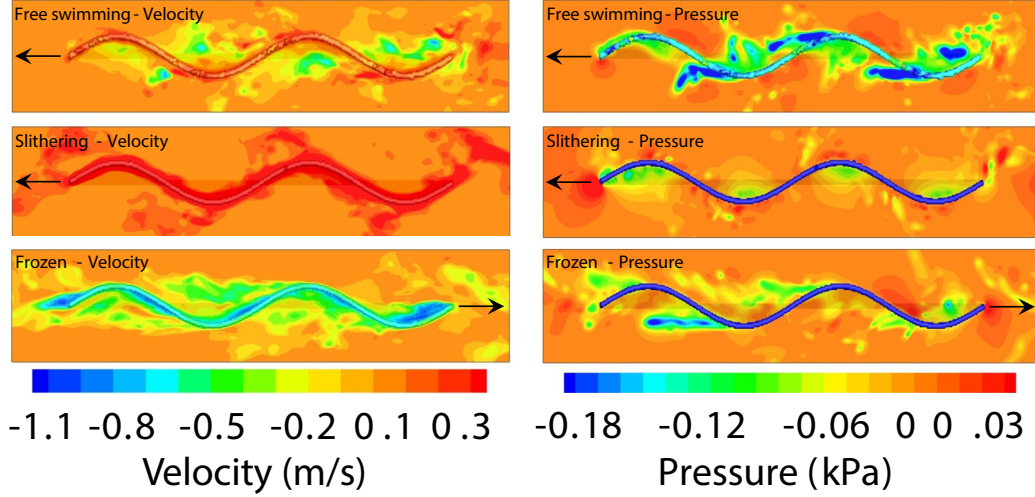


Figure 4. The axial velocity (left) and pressure (right) fields in a cross-sectional plane at the bottom edge of the ribbon fin for three cases. Top: Normal case with $U = 3$ cm/s and $U_w = 15$ cm/s. Middle: Perfect slithering motion with $U = 15$ cm/s and $U_w = 15$ cm/s. Bottom: Frozen fin motion with a backward (i.e. to the right) velocity of 12 cm/s. The legend for axial velocity (left) show magnitudes that are scaled by $U_w = 15$ cm/s. In the contour plot velocity to the left (i.e. forward direction) is positive and to the right (backward) is negative. The legend for pressure (right) show magnitudes scaled by ρU_w^2 where $U_w = 15$ cm/s.

Thus, we have two new results: first, an approach to separate the mechanisms of drag and thrust, and second we obtain a correlation not only for the thrust (Fig. 3c) but also for the drag (Fig. 3b) on an undulatory propulsor.

2.3 The spatial segregation of drag- and thrust-related flows

Consider a ribbon fin moving with $U = 3$ cm/s and $U_w = 15$ cm/s. Through simulation, the total forward force is found to be 0.46 mN. The drag causing perfect slithering mode has $U = 15$ cm/s and $U_w = 15$ cm/s. The thrust generating frozen mode has no wave velocity but has a backward velocity of $U_w - U = 12$ cm/s. Separate simulations were conducted for the drag and thrust causing modes. The calculated thrust and drag forces were 0.92 mN and 0.52 mN, respectively. The difference is 0.4 mN which is close to 0.46 mN computed for the un-decomposed case, i.e., Eqn. 1 is approximately satisfied. We plot the simulated axial velocity and pressure for these three cases in Fig. 4 for the same phase of the fin. The slithering drag mode has thin boundary layers outside of which the velocity has low magnitude and does not have strong spatial gradients. On the other hand, the frozen thrust mode has strongly

separated regions behind the troughs and crests of the wave along the fin. This velocity field and its gradients are significant *outside* the boundary layer region of the slithering mode. Wherever the velocity due to one mode is high, the velocity due to the other mode is low. The coupling of the drag and thrust causing modes, through the nonlinear inertia term $((\mathbf{u} \cdot \nabla)\mathbf{u})$ in the Navier–Stokes equations (equation 18), is weak. Furthermore, Fig. 4 shows that the dominant pressure regions due to the two modes are also spatially segregated. The low pressure due to the thrust-causing frozen fin mode is dominant behind the wave troughs and crests, whereas the low pressure due to the slithering mode is dominant away from the separation region in the concave part of the wave shape. This spatial segregation of the drag– and thrust–related flows is the fundamental basis of the success of the drag–thrust decomposition.

Finally, we note the contributions to the force from pressure and viscous terms. Due to separation, the pressure contribution to the thrust force dominates in the thrust causing frozen fin mode. Of the total thrust force of 0.92 mN, the pressure contribution is 0.81 mN and the remainder is due to the viscous contribution. In the drag causing slithering mode the viscous contribution is 0.12 mN out of the total drag force of 0.52 mN and the remainder is due to the pressure contribution. Thus, the pressure force dominates thrust while the viscous contribution to drag is relatively large due to thin boundary layers.

It has long been hypothesized that the drag of swimming fish is higher due to the thinning of the boundary layers caused by undulatory motion [10]. Fig. 4 shows that the boundary layer flow is a key feature of the drag causing slithering mode. Separated flow plays a role in the thrust mechanism. The separated flow regions are suction zones where the fluid is sucked backward by the undulating fin. This leads to the thrust force. This is consistent with our flow visualization data reported earlier [14, 15].

2.4 Generality of the drag–thrust decomposition

The decomposition described above was applied to an idealized ribbon-fin with idealized kinematics at a Reynolds number around 10,000. This idealization may not be valid for swimming animals, thus we now examine the applicability of the drag–thrust decomposition to swimming animals with realistic body/fin geometries and measured kinematics. We also examine the validity of the decomposition at moderately high Reynolds numbers by applying the decomposition to a robotic knife-fish.

2.4.1 Application to swimming animals

Our kinematic decomposition of drag and thrust assumed a constant amplitude wave (Fig. 2). This assumption is not strictly valid for swimming animals. For example, in the black ghost knifefish the amplitude of oscillation of the ribbon-fin tapers-off toward the two ends [9]. Anguilliform and carangiform swimmers have an amplitude that increases with body length [16–18]. Additionally, the wave motion may not be strictly sinusoidal. In the non-constant amplitude case, the kinematic split as proposed in this work will not be exact. However, if the amplitude changes are not large then the additional error may not be significant. The approach is expected to work in cases where cross-sections (width of the body in the lateral direction) of the body are non-uniform, provided that the body width does not change sharply along the body. The proposed decomposition is not expected to work for indefinitely high Reynolds numbers, but it does work at moderately high Reynolds numbers which will be demonstrated in the next subsection. Finally, as the height of the ribbon-fin and its amplitude of oscillation is reduced, the drag and thrust producing flow fields may not remain as separate as the case shown in Fig. 4. Thus, as the undulatory propulsor becomes slender the decomposition of drag and thrust may not be as clear. Given these issues, we examine the applicability of the decomposition with simulations of the eel *Anguilla rostrata*, the larval zebrafish *Danio rerio*, the black ghost knifefish *Apteronotus albifrons*, and the mackerel *Scomber scombrus*. These examples show where the decomposition is valid, and where it becomes invalid.

The drag, thrust, and undecomposed forces on a black ghost knifefish (gymnotiform), an eel (anguilliform), a larval zebrafish (sub-carangiform), and a mackerel (carangiform) are tabulated in Table 1. Table 1 shows that the error in decomposing forces on free swimming knifefish, eel, and zebrafish is small compared to that in decomposing the force on a mackerel. During steady free swimming, the average force in the swimming direction is zero. For a steady free swimming organism, the drag and thrust components must be equal. For the black ghost knifefish and the larval zebrafish, it is seen that the drag and thrust forces are equal to each other within 5%. Note that the knifefish displays a small variation in amplitude whereas the zebrafish has a subcarangiform amplitude variation. For the eel, which has an anguilliform amplitude variation, the drag and thrust forces are equal with an error of 17% (Table 1). Thus, we see that our decomposition works well for gymnotiform (and by similarity for balistiform and rajiform), anguilliform, and subcarangiform swimmers, none of which display rapid variations in amplitude. But, the decomposition does not work well for carangiform swimmers because the rate of change of amplitude in these swimmers is very high (Table 1). A theoretical assessment of why the decomposition works well

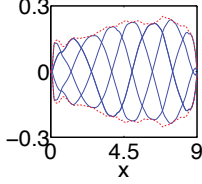
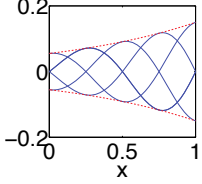
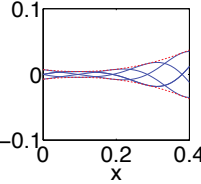
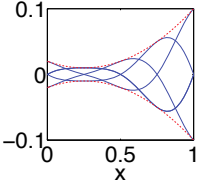
	Knifefish	Eel	Zebrafish (larval)	Mackerel
Amplitude (cm)				
Amplitude function $A(x)$	Experimental [9]	$0.15e^{(x-1)}$ [17]	Experimental	$0.02 - 0.08x + 0.16x^2$ [16, 18]
Thrust force T (mN)	1.43	6.8×10^{-4}	4.3×10^{-3}	11.6×10^{-3}
Drag force D (mN)	1.48	8.2×10^{-4}	4.1×10^{-3}	46.8×10^{-3}
Undecomposed force F (mN)	0	0	0	21.4×10^{-3}
Net force $D - T$ (mN)	0.05	1.4×10^{-4}	-0.2×10^{-3}	35.2×10^{-3}

Table 1. Drag-thrust decomposition of free swimming black ghost knifefish fin, eel, larval zebrafish. Also shown is the decomposition of a hypothetical fin with mackerel kinematics. The amplitude shown for the knifefish is at distance of 0.75 cm from base of the fin. The range for x in $A(x)$ is $[0, 1]$. Undecomposed forces equal to zero indicate free swimming cases.

for modest variations in body or fin amplitude along the body length, but not for large variations in amplitude, is presented in the Discussion Section.

2.4.2 Application to a robotic knifefish

Here we examine how well the decomposition works at moderately high Reynolds numbers. We consider parameters for a robotic knifefish, approximately three times longer than the adult live knifefish. At typical kinematic parameters, such as two waves along the fin undulating at 2.5 Hz, the Reynolds number based on fin length is around 130,000. Decomposition of drag and thrust forces on ribbon-fins at the scale of the robot was tested using simulations and experiments with the robot. The fin has the same dimensions and kinematic parameters in the simulation and the experiment. However, the surface of the experimental fin departs from the simulated fin in a manner that appears to affect our results, as will be described later.

Simulations of the decomposition were carried out for a fin the same size as that on the robot, but without a body. In section B and Fig. 13 we show that the forces on the body and the fin are decoupled, and the presence of the body has no influence on the fin forces. Hence, the decomposition can be carried out with or without the body. We choose to carry out the decomposition without the body to reduce the computational cost. We consider a case where $U = 0$ cm/s and $U_w = 40.75$ cm/s. The net force generated by the fin was found to be 384.7 mN. In the drag causing slithering mode, the fin translated forward at $U = U_w = 40.75$ cm/s. In the thrust-causing frozen mode the fin translated backward with a velocity of $U_w - U = 40.75$ cm/s (slithering and frozen velocity are same because $U = 0$ cm/s in the undecomposed mode). Thrust and drag forces were found to be 427.1 mN and 33.54 mN, respectively. The difference between thrust and drag force (393.46 mN), matches well with the force of the undecomposed mode (384.7 mN). Based on simulations, we infer that the drag-thrust decomposition is valid at length scales of robotic knifefish's ribbon-fin.

As noted before, the parameters used in the experiments were same as those used in simulations, above. Forces in the undecomposed, slithering (drag), and frozen (thrust) modes were measured to be 226.8 mN, 229.5 mN, and 283.3 mN respectively. The difference between drag and thrust force is not equal to the undecomposed force. The undecomposed force and thrust force are of the same order of magnitude just as it is in simulations. This raises two important questions: i) what is the source of the larger than expected slithering (drag) mode force? ii) given this disagreement, is there a resolution?

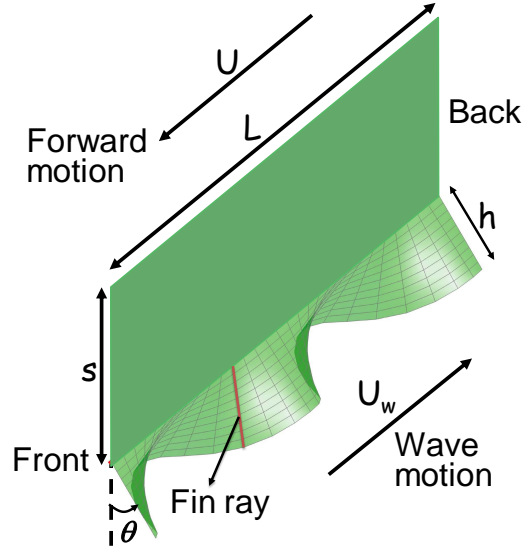


Figure 5. Geometric parameters and the configuration of the plate-fin assembly.

These questions will be addressed in the Discussion Section.

2.5 Utility of the drag–thrust decomposition

2.5.1 Optimal height of a knifefish ribbon fin

What is the utility of separating drag and thrust in the manner we have proposed? Next we show that this decomposition provides a powerful predictive tool. To that end, we consider a specific example problem: given the body of a knifefish, which is held nearly rigid, what should be the height of its ribbon fin? We also show how drag–thrust decomposition leads to models that can predict the swimming velocity of an organism.

To find the preferred fin height, we hypothesized that the observed height of the ribbon fin is such that the mechanical energy spent per unit distance traveled, referred to as the mechanical cost of transport (COT), is minimized. The COT was computed numerically for different fin heights as discussed below. We considered steady swimming in which a fish moves with a constant mean velocity. For simplicity, we considered a plate–fin configuration like that used by Lighthill and Blake [12] to study gymnotiform and balistiform swimming. A plate of height $s = 2$ cm and length $L = 10$ cm was attached to a ribbon fin of the same length (Fig. 5). These dimensions were selected based on typical fin and body heights

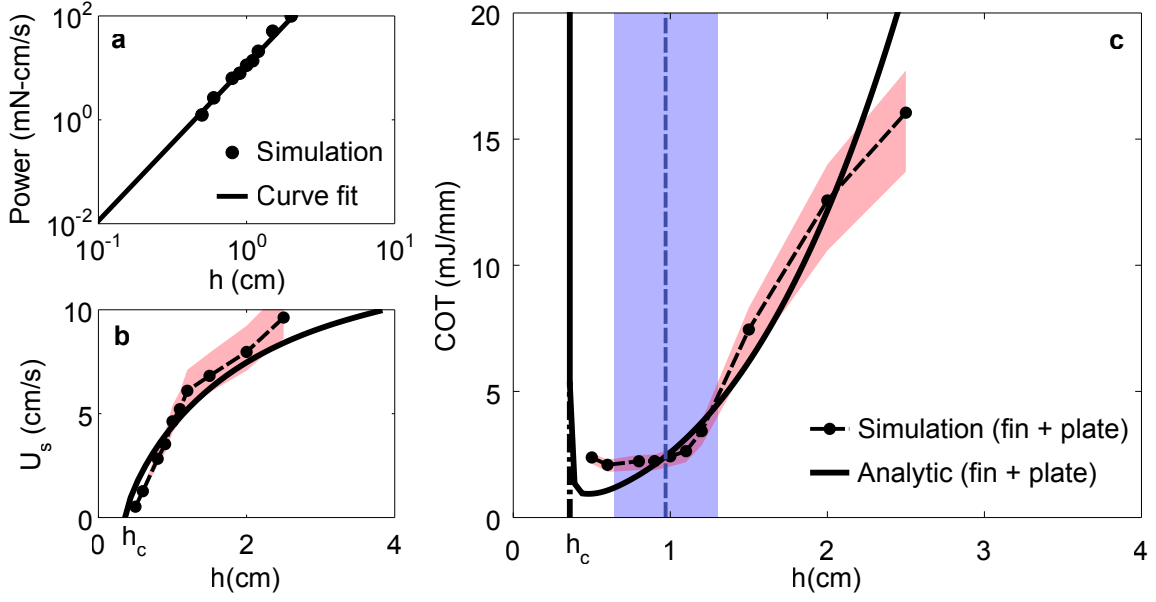


Figure 6. a) Mechanical power expended in the fluid, obtained from fully resolved simulations of self-propulsion, as a function of the fin height. b) Swimming velocity as a function of the fin height h obtained from fully resolved simulation of self-propulsion as well as from a reduced order model (solid line). c) The mechanical cost of transport as a function of the fin height h obtained from fully resolved simulation of self-propulsion as well as from a reduced order model. The red shaded region represents the variation of swimming velocity in (b) and cost of transport in (c) due to a perturbation to the plate height. The perturbation to the height is equal to ± 0.85 cm, which corresponds to the standard deviation of the measured body heights in an assortment of knifefish at the half way point along the fin (see Table 3). The dashed blue vertical line in (c) corresponds to the mean fin height measured, and the blue shaded region represents the standard deviation in fin height. Note: The closed circle and the solid line in (b) and (c) have the same meaning.

in adult knifefish [9, 13, 19]. The following kinematic parameters were chosen: $\theta_{\max} = 30^\circ$, $f = 3$ Hz, $\lambda = 5$ cm. The fin height was varied from 0.5 cm to 2.5 cm. For each fin height we solved the problem of self-propulsion by using a previously developed efficient algorithm [20]. In these computations the traveling wave motion of the ribbon fin attached to the plate was specified. For each case we computed the mean power P spent by the fin against the fluid over one period of the steady swimming cycle. The time-averaged swimming velocity U_s was estimated during steady swimming. The cost of transport was computed as $\text{COT} = P/U_s$.

Fig. 6 shows plots of the swimming velocity U_s , the mean power P , and COT as a function of the ribbon fin height h . The power spent on the fluid follows a power law trend (Fig. 6a). The swimming velocity U_s first increases rapidly with respect to h and then changes slowly at higher values of h (Fig. 6b).

This trend is a direct result of different scalings of drag and thrust forces with respect to h (Section B). The COT is low and nearly constant at smaller h after which it grows rapidly (Fig. 6c). The basis of this increase in COT is that at larger h , the power increases with increasing h but the corresponding increase in U_s is small. Hence there is a rapid growth of COT at larger h . Fig. 6c shows that the ribbon fin heights that give lower values of COT, for a plate height of 2 cm, are in the range of 0.5 – 1.1 cm. In this range the COT does not change significantly but the swimming velocity is highest at $h = 1.1$ cm. In short, different scalings of drag and thrust with respect to h lead to a specific trend of U_s vs. h , which in turn determines the trend of COT vs. h . The COT trend eventually provides the prediction for the fin height h that will minimize the metabolic cost of movement, and as we will see in the next section, this predicted height agrees well with observed fin heights.

Sensitivity of the optimal fin height to fish body size: The predicted fin height (~ 1 cm) is consistent with the mean fin height of 0.97 cm that we measured for 13 species in 8 genera in the family Aptereronotidae of weakly electric South American knifefishes (Table 3, at 50% body length). The standard deviation of the fin height from the measured mean value (blue vertical bar in Fig. 6c) is within the range of fin heights (0.5 – 1.1 cm) for which COT is predicted to be low. Although the body height of the fishes we considered did vary, we found from a sensitivity analysis (see Section C) that the influence of the plate (or body) height on the COT trend is not significant. We show this result in Fig. 6c, where the red shaded region shows the variation in COT due to a change in plate height corresponding to the standard deviation in the body height of the 13 species we measured.

2.5.2 Prediction of swimming velocity

Finally, to show that the proposed drag-thrust decomposition can be used to predict swimming velocities, a force balance equation similar to Eqn. 1 was written for the steadily swimming fin-plate assembly (Eqn. 13). We used that equation to derive an analytic solution for the fin height as a function of swimming velocity (Eqn. 15), which can be rearranged to give swimming velocity as a function of fin height. To test the analytic prediction of swimming velocity we performed numerical simulations to compute the swimming velocity. Excellent agreement between the analytic and numerical solutions of swimming velocity is shown in Fig. 6b.

3 Discussion

3.1 Are there other ways to obtain drag–thrust decomposition?

There can be many kinematically consistent decompositions which satisfy kinematic conditions D1 (body movements creating drag summed to body movements creating thrust result in the original undecomposed movement) and D2 (body movements creating drag and thrust are without discontinuities and physically realizable). However, the kinematic decomposition depicted in Fig. 2 is the only one we have found satisfying D1 and D2 as well as providing force decomposition (D3, the sum of the decomposed drag and thrust forces is equal to force in the originally observed swimming motion of the animal). The primary reason that force decomposition becomes possible is due to boundary layer flow in the drag mechanism and separated flow in the thrust mechanism (Fig. 4). A boundary layer flow is observed in the drag mechanism because in that case the velocity on the fin surface is tangential to the surface itself (Fig. 4). This type of internal boundary condition arises because the forward translational velocity of the fin in the slithering mode is equal and opposite to the wave velocity of the undulating fin. Any translational velocity in the drag mode that is other than U_w will result in a velocity at each point on the fin that is no longer tangential to the surface. This gives rise to a flow field that is not purely due to the boundary layer and it couples with the separated flow field due to the thrust mechanism. Thus, even if other decompositions are kinematically correct, the force decomposition will not work well. The kinematic decomposition that we have is the one that leads to the least coupling between the drag and thrust modes for the kinematics considered here.

As an example, consider a different kinematic decomposition where the backward traveling wave is *defined* as the thrust producing mechanism whereas the fin translating forward with velocity U is *defined* as the drag producing mechanism. We used our data to check if this kinematic decomposition also leads to force decomposition. If valid then it should be possible to split the total force as

$$F[U, U_w] = T_s[U_w] - D_f[U], \quad (2)$$

where $T_s[U_w]$ is the forward force on a *stationary* fin with traveling waves moving backward with wave velocity U_w , and $D_f[U]$ is the force on a fin with a fixed shape, i.e. the *frozen fin*, that is translating forward with velocity U . Using the data for F in Fig. 3a and the data for $D_f[U]$, available from our frozen

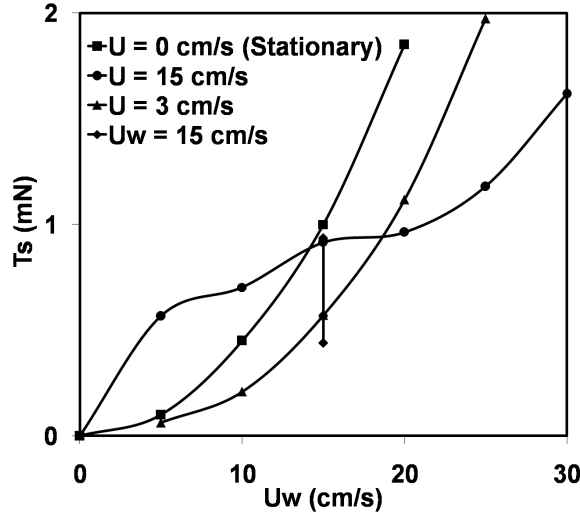


Figure 7. The thrust force T_s computed as a function of U_w for each data point in Fig. 2 by assuming a decomposition according to equation 2. In this case the data do not cluster along a single curve. The legend identifies different simulation sets. For example, the set with $U_w = 15$ cm/s was the one where U_w was fixed and the value of U was changed.

fin simulations, we computed $T_s[U_w]$. These values are plotted in Fig. 7 and compared to the force on a stationary ribbon-fin from our prior work [14]. If this decomposition is valid, all data should fall on a single curve in Fig. 7. That is not the case. It can be shown that the reason this decomposition does not work is because the corresponding flow fields are not decoupled.

Given that drag and thrust appear intermingled in swimming organisms, especially in the undulatory mode, it has been hypothesized that there must be some spatial or temporal separation between thrust and drag production that allows the total force to be zero on average over a swimming cycle [17]. A model to estimate thrust based on temporal oscillations of the swimming velocity has been proposed [21]. Our data suggests that a decomposition of the total force into drag and thrust is possible without relying on spatio-temporal splitting.

3.2 Comments on different measures of drag reported in literature

Appropriate measures of drag on a swimming organism have been debated in literature for many decades [22, 23]. Here, we discuss how drag from our decomposition differs from definitions of drag in the literature. One measure that has been used is the tow-drag, i.e., the drag on a non-swimming organism if it is pulled in the fluid at its swimming velocity. The organism is usually not deformed in these experiments

or theoretical estimates. This drag measure is not expected to be correct because the shape of the animal for the tow-drag estimate does not match with shape of the fish during propulsive movement [22]. The second measure is the drag obtained by pulling a deformed non-undulating body through the fluid at its swimming velocity, i.e., the drag on the frozen shape configuration. As noted above and in Fig. 7, this does not result in successful decoupling of thrust from drag. Our results suggest that an appropriate drag measure for undulatory propulsion is the one corresponding to the perfect slithering motion at the wave velocity (Fig. 4).

These measures are best illustrated by considering a hypothetical swimming ribbon-fin with no body attached to it. According to the drag-thrust decomposition and the data in Figures 3b and 3c, a ribbon-fin with $U_w \approx 22$ cm/s will swim with a velocity $U \approx 9.5$ cm/s. The first drag measure - the tow-drag - for this case corresponds to the drag on a flat plate towed at 9.5 cm/s. This is estimated to be 0.12 mN based on boundary layer theory. The second drag measure corresponding to a frozen fin, moving at 9.5 cm/s, is 0.6 mN. Finally, the third drag measure proposed by us corresponding to the perfect slithering motion with $U_w \approx 22$ cm/s is 1 mN. Thus, our drag measure is higher than the other two estimates for the scenario considered here. The result is consistent with reports in literature that the tow-drag is often found to be lower than that required to achieve a balance of drag and thrust forces during swimming [22, 23]. In general, however, the relative magnitudes of the three drag measures may not be in the same order as in the example discussed above. It will depend on various parameters including the geometric configuration.

It has been noted in the past that body undulations lead to a reduction in drag on a swimming body [24]. That conclusion was based on computing the total force on an infinite two-dimensional wavy surface for a given imposed velocity U and then noting that as U_w is increased the total force changes from being backward (drag-like) to being forward (thrust-like). In this sense the presence of undulations reduces the drag-like behavior. This is consistent with our results.

3.3 Limits of the drag–thrust decomposition

Results of the decomposition of forces on swimming animals showed that the decomposition is valid for swimming animals with anguilliform, gymnotiform (by similarity balistiform and rajiform), and sub-carangiform kinematics. But, the decomposition is not valid for swimming animals with carangiform kinematics. Here, we present a theoretical assessment of when the proposed decomposition will be correct and when it will fail. For the purpose of analysis, consider kinematics imposed on a rectangular

surface (“fin” hereafter) of infinitesimal thickness. At any instant a given point on the fin undergoes lateral displacement given by

$$y = A(x) \sin[2\pi(\frac{x}{\lambda} + ft)], \quad (3)$$

where $A(x)$ is the amplitude which is a function of axial direction and it determines the mode of swimming. The amplitude for different modes of swimming is shown in Table 1. The deviation from exact decomposition is a function of the rate of increase of amplitude with body length. The deviation will be more if the rate of amplitude change is high and vice-versa. This will be demonstrated below.

The slithering mode is affected by a deviation from exact decomposition. The slithering mode has the property that velocity at each point on the fin is tangential to surface of the fin. The velocity in the slithering mode, at a point, is the resultant of the forward translational velocity U_w and the lateral velocity V_w . The angle, α (Fig. 2), of the velocity at a point is given by

$$\tan \alpha = \frac{2\pi A(x) \cos[2\pi(\frac{x}{\lambda} + ft)]}{\lambda}. \quad (4)$$

The direction of the resultant velocity at every point on the fin surface must be equal to slope of the corresponding point if the velocity has to be tangential to the fin surface. The slope of a point on the fin undergoing traveling wave motion is given by

$$\frac{dy}{dx} = \frac{2\pi A(x) \cos[2\pi(\frac{x}{\lambda} + ft)]}{\lambda} + \frac{dA(x)}{dx} \sin[2\pi(\frac{x}{\lambda} + ft)]. \quad (5)$$

Note that if $A(x)$ is constant then equation 4 and 5 are identical resulting in a perfect slithering motion where the resultant velocity of a point is tangential to the fin surface. Substituting equation 4 in 5 we get the following equation

$$\frac{dy}{dx} - \tan \alpha = \frac{dA(x)}{dx} \sin[2\pi(\frac{x}{\lambda} + ft)]. \quad (6)$$

The above equation is a measure of deviation from exact decomposition. At a given instant of time, the deviation from tangential velocity is directly proportional to $\frac{dA(x)}{dx}$. The figures in the first row of Table 1 show that the rate of amplitude change in anguilliform swimmers, subcarangiform swimmers and knifefish is slower than that in carangiform swimmers. In anguilliform swimmers the amplitude gradually increases from head to tail, i.e, the rate of change of amplitude is smaller. Thus, the deviation from perfect slithering motion is small. The same is true for the subcarangiform swimmer as well. In case

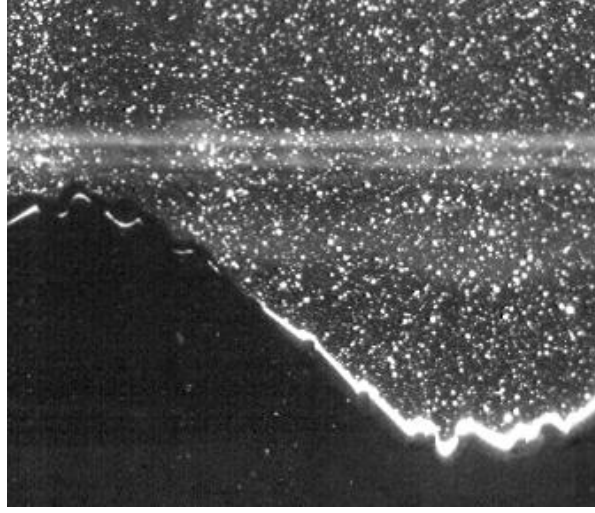


Figure 8. The surface of the robotic ribbon fin during sinusoidal undulations. The material between adjacent rays folds and results in kinks on the fin surface.

of the knifefish amplitude, the amplitude first increases, reaches a peak, and then decreases. But the rate at which amplitude increases or decreases is very small, hence the deviation from perfect slithering motion is small. Thus, the decomposition of eel, larval zebrafish and knifefish worked well. However, in carangiform swimmers, the amplitude remains relatively small and constant for at least half the body length after which it increases rapidly. The rate of change of amplitude is very high towards the caudal portion of the body thus resulting in a large deviation from perfect slithering motion. Consequently, it is not surprising that the decomposition did not work for mackerel.

3.4 Why the drag–thrust decomposition failed for the robotic knifefish

Using numerical simulations it was shown that the decomposition was valid for the robotic knifefish. But, experimental data did not agree with the simulations. The main difference between the experiments and the simulation was in the force of the slithering mode. The slithering drag force from experiment was higher than that from simulation; this implies that the drag force is higher than what it should be for the decomposition to be valid. We hypothesize that the larger than expected slithering drag force in the experiment is due to the imperfections on the robot’s fin surface. The robotic fin is made up of discrete rays (32 rays 1 cm apart) that are connected by Lycra fabric; see Fig. 10 in which one of the fin rays is highlighted in white. It is not possible to produce a smooth sinusoidal wave on the fin unless the fin is

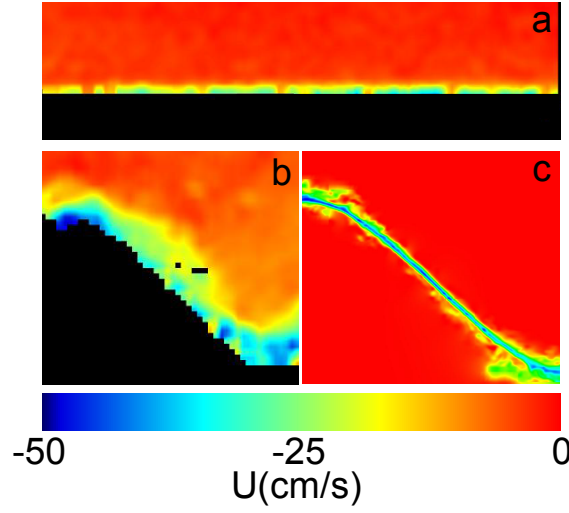


Figure 9. A comparison between the boundary layer due to, a) flow past a flat plate, b) slithering motion of a robotic ribbon fin, c) and slithering motion of a modeled robotic fin in a simulation. The boundary layer is shown on a horizontal plane 1 cm above the bottom edge of the fin toward the robot body. The color bar represents the axial velocity.

made up of very large number of rays. Owing to the limited number of rays, the sinusoidal wave generated by the robotic fin is not smooth (see Fig. 8). With kinks on its surface the robotic fin cannot maintain a thin boundary layer in the slithering mode like that in simulations. The kinks will introduce disturbances into the boundary layer (see Fig. 9). Unlike its real counterpart, the robotic fin modeled in the simulation is composed of very fine grid points (whose resolution is of the order of fluid grid resolution). Any curved surface can be imposed (sinusoidal or otherwise) on the modeled fin surface without causing any kinks. Hence, it leads to a thin undisturbed boundary layer in the slithering mode (see Figure 9). The boundary layer on the robotic fin is very thick when compared to that from simulation or that from flow past a flat plate at the same Reynolds number (see Figure 9). The large thickness of the boundary layer may also indicate separated flow, which could lead to the large drag force measured in the experiment.

3.4.1 An alternate estimate of the drag force on the robotic ribbon fin

Given that the slithering mode force in the experiment does not satisfy the drag–thrust decomposition due to disturbances caused by surface kinks, we propose that the next best choice may be to use a drag estimate that is similar to the tow–drag. This is because the surface imperfections on an undeformed (or straight) robotic ribbon–fin would be much less and consequently the flow would be less perturbed or

separated. There is subtle, yet important, difference between our estimate of drag and the conventional measure of tow-drag. In the conventional measure of tow-drag, the swimmer is towed at its swimming speed in stationary water. In contrast, we measure the drag by towing a straight fin, in stationary water, at the velocity of the slithering mode (which is equal to wave velocity, $U_w = 40.75$ cm/s) instead of swimming speed. The force was measured to be 81.9 mN. This value is closer to the expected value of 56.6 mN obtained from the drag thrust decomposition estimate.

3.4.2 Why the drag–thrust decomposition works for real knife-fishes

Simulations have shown that the decomposition is indeed valid at moderately high Reynolds number. Experiments on the robotic knife-fish, however, suggest possible limitations of the decomposition. The decomposition is sensitive to any deviation from perfect slithering mode, be it due to high levels of amplitude change or high roughness on the fin surface. A knife-fish’s ribbon-fin is composed of 120–320 rays spanning fin lengths of 10–30 cm, giving typical densities of about one ray per millimeter (Table 4 and Fig. 41 of [25]). Many of these fin rays branch into two rami half the way from their base to their distal ends, which would effectively double the ray density along the very portion of the fin surface that could become uneven due to spreading between the rays when they are oscillated [25]. With such fine ray spacing, a knife-fish can produce curved surfaces on its fin without kinks. In contrast, on the robot the ray density is one ray per 10 mm, resulting in a much less smooth fin surface. We therefore expect that drag-thrust decomposition would be applicable to a robotic ribbon-fin if it can be designed to have higher ray density so that the fin surface is smoother.

4 Methods

4.1 Experimental setup

4.1.1 Robotic undulating fin

The robotic model used for the experimental work was the ‘Ghostbot,’ a biomimetic knife-fish robot which undulates an elongated fin to generate thrust (see Fig. 10). The robot consists of a rigid cylindrical body that houses the motors and electronics to drive the individual rays of the fin. There are 32 rays to actuate a rectangular Lycra fin measuring 32.6 cm by 5 cm. More details of the robot are found in [26], with the

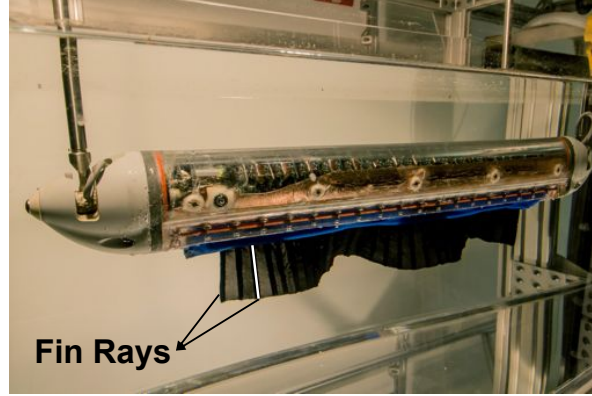


Figure 10. The robotic knife-fish used in the drag-thrust decomposition experiments. The robotic ribbon-fin is composed of 32 fin rays and a Lycra fabric connecting the rays. One of the fin rays is coloured white to highlight it.

only difference being the depth of the fin was 3.37 cm in the previous work rather than 5 cm.

4.1.2 Measuring hydrodynamic forces

The robot was suspended horizontally into a variable speed flow tank from an air-bearing platform allowing near frictionless motion in the longitudinal axis. We fixed the robot in the lateral and vertical directions. We placed a single axis force transducer (LSB200, Futek, Irvine, CA, USA) in the longitudinal axis between the air-bearing platform and mechanical ground, allowing us to measure the forces generated by the robot or acting on the robot along that axis. Voltages from the force transducer were recorded at 1000 Hz. For each trial, we allowed ample time for the hydrodynamics to reach steady state (30-60 seconds), then averaged the last 10 seconds of data, which was converted to force units based on the calibration, which had a maximum nonlinear error of 0.034%. The flow speed of the water tunnel was measured and calibrated using particle image velocimetry (PIV). More details on PIV are provided in the following section.

4.1.3 Particle image velocimetry (PIV)

We analyzed horizontal PIV planes to measure the boundary layer thickness caused by the fin. The PIV setup used is the same as the one described in [15]. In short, a 2 W laser beam (Verdi G2, Coherent Inc., Santa Clara, CA, USA) is scanned at 500 Hz to create a planar laser light sheet. A high-speed camera (FastCam 1024P PCI, Photron, San Diego, CA, USA) imaged reflective particles suspended in

the fluid (44 micron silver coated glass spheres, Potter Industries, Valley Forge, PA, USA) at 500 frames per second, matching the scanning rate of the laser. High-speed video was analyzed using a commercial software package (DaVis, LaVision GMBH., Göttingen, Germany). Successive frames of the video were cross-correlated to calculate the velocity vector field of the fluid. Cross-correlation consisted of two passes with decreasing interrogation windows, first with an interrogation window of 32 by 32 pixels with 50% overlap and second with a window of 16 by 16 pixels with 50% overlap.

4.2 Numerical problem formulation

For the numerical simulations, the ribbon fin is modeled as a thin membrane as shown in Fig. 1. The angular position $\theta(x, t)$ of any point on the fin (described above in under Results) is modeled as

$$\theta(x, t) = \theta_{\max} \sin 2\pi\left(\frac{x}{\lambda} - ft\right). \quad (7)$$

This corresponds to a sinusoidal traveling wave along the fin of length L and height h . Kinematic parameters are frequency f , θ_{\max} , and λ . The speed at which the wave form travels along the fin is called the wave velocity, $U_w = f\lambda$. In the optimal ribbon fin height analysis (presented in Results section), the knife-fish is modeled as a plate-fin assembly where a rigid plate is attached to the ribbon-fin in place of the fish's rigid body. In these simulations, the rigid plate is modeled as a rigid surface. The properties of water are used for the fluid. Two types of simulations are performed in this work. In one type, the translational velocity U of the fin and/or plate is specified along with the deformation kinematics of the fin (equation 7). These simulations are carried out in the frame of reference of the fin/plate. Hence the translational velocity U appears as an imposed free stream velocity. Rotation of the fin/plate is prohibited.

In the second type of simulation, only the deformation kinematics of the fin are prescribed, which result in a self-propelling fin-plate assembly. Complete details of the computational method and validation are given in [14, 20]. In this method, the viscous Navier-Stokes equations along with the incompressibility constraint are solved in the entire domain. The effect of the immersed fin/plate is resolved by a new constraint based formulation described in [20]. A finite difference method that is 6th order in space and 4th order in time is used. The grid size was chosen after performing a grid-sensitivity study. The Courant-Friedrichs-Lewy (CFL) number is 0.25 for all simulations. Periodic boundary conditions are

	Knifefish	Eel	Zebrafish (larval)	Mackerel
Body/Fin dimensions length×height (cm²)	Actual (9×1)	1×0.1	Actual (0.38×0.04)	1×0.2
Wavelength λ (cm)	3.75	1	0.31	1
Frequency f (Hz)	10.3	5	33.3	15.7
Fluid density (kg/m³)	1000	1000	1000	1000
Fluid viscosity (Pa s)	0.9×10^{-3}	1.4×10^{-5}	0.9×10^{-3}	0.9×10^{-3}
Wave velocity (cm/s)	38.62	5	10.32	15.7
Translational velocity (cm/s)	11.9	2.89	1.125	10

Table 2. Simulation parameters.

used in all directions. The computational domain was made large enough to minimize the impact of periodicity. Mean forces and power of the fin were calculated as the time average over at least one period of oscillation, after a quasi-steady state is reached.

Parameters chosen to match those of an adult black ghost knifefish [13] are: fin length $L = 10$ cm, fin height $h = 1$ cm, $f = 3$ Hz, $\theta_{\max} = 30^\circ$, and $\lambda = 5$ cm. The density and viscosity of water are taken as $\rho = 1,000$ kg/m³ and $\mu = 8.9 \times 10^{-4}$ kg/m·s unless otherwise specified.

4.2.1 Numerical simulations of swimming animals

Real three dimensional geometries of the bodies or fins were simulated in all cases except the mackerel where a sheet-like fin was simulated with mackerel-like kinematics. The simulation parameters and the kinematics are given in Table 2. The fin profile and the kinematic data of the knifefish were experimentally obtained by us [9]. Only the ribbon-fin of the knifefish was considered for the decomposition. The body of the knifefish was not considered for the same reason the body was not considered in the robot simulation. Experimentally extracted kinematic data and body profile of the larval zebrafish were provided by Melina Hale of The University of Chicago. The body profile of the eel was taken from Kern and Koumoutsakos’



Figure 11. The lines along which the fin length, fin height, and body height were measured for *Aptereronotus albifrons*. Scale bar: 10 mm.

[27] analysis of anguilliform swimming. The kinematics of both the mackerel and eel were described by equation 3, where the amplitude of kinematic undulations are based on experiments. Eel kinematics were based on experiments by Tytel and Lauder [17], and mackerel kinematics were based on experiments by Videler and Hess [16].

4.2.2 Sign convention

As shown in Fig. 5 the forward direction is to the left and the backward direction is to the right. Translational velocities U and U_s are positive if directed to the left (forward) while the wave velocity U_w is positive if directed to the right (backward). All forces considered in this work are parallel to the length of the plate and the fin. Thrust force *on* the fin is positive to the left while drag forces *on* the fin and plate are positive to the right. The resultant force *on* the fin due to thrust and drag is positive to the left.

4.3 Measurements of fin and body size of South American weakly electric fishes

A group of 13 species in 8 genera in the family Aptereronotidae of South American weakly electric fishes were considered. The family Aptereronotidae is one of five families encompassing 32 genera and 135 species of South American knifefishes [28]. We restricted our measurements to a subset of one family for practical reasons, but it is evident from illustrations and images of knifefish in other families that the Aptereronotidae are quite typical in terms of the body height to fin height issue examined here [25, 28, 29].

An image of each specimen was provided by Andrew Williston of the Museum of Comparative Zoology,

Genus	Species	Sp. ID	BL	BLF	FL	25% FL			50% FL			75% FL		
						S	H	R	S	H	R	S	H	R
Adontosternarchus	devanazii	59522	8.30	10.00	7.20	1.10	0.60	1.83	0.86	0.65	1.32	0.45	0.50	0.90
Adontosternarchus	clarkae	78151	8.30	8.30	7.40	1.20	0.60	2.00	0.92	0.63	1.47	0.98	0.43	2.27
Adontosternarchus	sachsi	92914	11.70	15.80	10.50	1.40	0.62	2.26	1.12	0.68	1.65	0.66	0.50	1.32
Apteronotus	leptorhynchus	48686	10.90	12.80	9.40	1.82	0.60	3.03	1.49	0.71	2.10	0.80	0.71	1.13
Magosternarchus	duccis	46884	11.20	13.00	10.50	1.80	0.78	2.31	1.50	0.73	2.05	0.90	0.65	1.38
Apteronotus	bonapartii	78152	14.10	16.70	12.30	2.00	0.60	3.33	1.60	0.65	2.46	0.90	0.53	1.71
Sternarchella	schotti	59517	14.80	17.20	12.90	2.04	0.87	2.34	1.60	0.95	1.68	0.98	0.73	1.34
Sternarchella	terminalis	98361	14.80	15.60	12.40	2.30	1.00	2.30	1.80	1.06	1.70	1.10	0.97	1.13
Portergus	gimbeli	164198	15.70	15.70	14.50	2.10	1.06*	1.98	1.85	1.05	1.76	1.25	0.83	1.51
Apteronotus	albifrons	78148	12.90	12.90	10.20	2.40	0.83	2.91	1.95	0.99	1.97	1.10	0.95	1.16
Sternarchogiton	porcinum b	164197	17.50	20.50	14.70	2.40	1.15	2.09	2.00	1.20	1.67	1.10	0.60*	1.83
Apteronotus	albifrons	169184	16.40	19.50	13.50	3.10	0.93	3.35	2.40	1.10	2.18	1.40	1.10	1.27
Sternarchorhamphus	muelleri	59514	33.00	39.70	26.90	3.88	1.75	2.22	2.82	1.53	1.84	1.80	1.26	1.43
Orthosternarchus	tamandua	98368	35.60	35.60	28.10	4.34	1.67*	2.60	4.18	1.64	2.55	2.90	1.10	2.64
Mean						2.28	0.93	2.47	1.86	0.97	1.89	1.17	0.78	1.50
Standard Deviation						0.94	0.38	0.50	0.85	0.33	0.35	0.59	0.26	0.47

Table 3. Body length (BL), body length with filament (BLF), fin length (FL), body height (S), fin height (H), ratio of body height to fin height (R) of 13 species across 8 genera of South American weakly electric fishes in the Apteronotidae, in order of body height at 50% along fin length. Specimen identification numbers (Harvard Museum of Comparative Zoology) are represented by Sp. ID. Body height, fin height, and their ratio (R) were measured at 25, 50, and 75 percent along the fin length, and the same are tabulated. Note: All lengths are in centimeters, asterisk indicates that the quantity in question was estimated, not measured.

Harvard University. The fin and body height measurements were made at three locations along the fin length from the rostral tip: 25, 50, and 75 percent. The height of the fin was measured by measuring the length of the collapsed fin ray. The height of the body was measured along a line that was perpendicular to the body axis. The lines of measurement are shown in Fig. 11. The measured data are tabulated in Table 3. For specimens in which fin rays were not present for measurements at a needed position along the fin, ray length was estimated based on the trend of neighboring fin ray lengths. These data points are marked by an asterisk in the table.

Acknowledgments

This work was supported by NSF grants CBET-0828749 to N.A.P. and M.A.M, CMMI-0941674 to M.A.M. and N.A.P, and CBET-1066575 to N.A.P. Computational resources were provided by NSF's TeraGrid Project grants CTS-070056T and CTS-090006, and by Northwestern University High Performance Computing System – Quest.

Author contributions

NAP, AAS, RB, MAM, and IDN conceived and designed the research and experiments. RB and AAS performed numerical simulations. IDN and RB performed experiments. NAP, RB, AAS, and MAM analyzed data. AAS, APSB, and NAP contributed the numerical simulation tool. IDN and MAM contributed the experimental tool. NAP, RB, AAS, and MAM wrote the paper. All authors edited the paper.

Appendices

A Difference between this work and Lighthill's approach

Our approach is different from prior work by Lighthill [10–12] for the following reasons: **1)** Our kinematic decomposition ensures that the realizability condition D2 (the decomposed body movements should be such that the surface of the body will move in a continuous fashion so that the kinematics can be realized in experiments or simulations) is satisfied, unlike Lighthill's decomposition. Thus, our decomposition allows setting up independent sets of simulations/experiments to determine the drag and thrust components. **2)** We show that the force condition D3 (the sum of the drag and thrust forces from the decomposed body movements must be equal to the force due the original body movement of the swimmer) is satisfied based on our approach. Because Lighthill's approach did not satisfy condition D2, this verification has not been possible. **3)** We are able to estimate both thrust and drag, unlike Lighthill's work where appropriate drag estimates are not available. Lighthill's approach for the decomposition of drag and thrust is summarized below.

Consider a generic surface with a traveling wave as shown in Fig. 12. It could represent the body of a swimmer or the surface of a fin. Consider the wave to have a constant amplitude and that the wave is traveling from left to right (i.e. backward) with velocity U_w which is constant. Due to the wave motion, any point on the surface oscillates laterally (or oscillates laterally along a figure eight-shaped path if the body is assumed inextensible [10]) with velocity $V_w = -2\pi f A \sin[2\pi(x/\lambda - ft)]$, where A is the amplitude of the wave, f is the frequency, x is the axial location of the point, and λ is the wavelength. It follows that $U_w = \lambda f$. Let U be the forward translational velocity (i.e. to the left; Fig. 12) of the surface as a whole and let the surrounding fluid be stationary. Positive values of U_w will imply a backward traveling wave whereas positive values of U imply a forward translating surface. The resultant velocity at any point on the surface is V as shown in Fig. 12. Lighthill [11] considered the components of V that are tangential (u) and normal (w) to the surface of the wave with large amplitude oscillations. It can be shown that

$$w = (U_w - U) \sin[\alpha], \quad (8)$$

$$u = \frac{U_w}{\cos[\alpha]} - (U_w - U) \cos[\alpha], \quad (9)$$

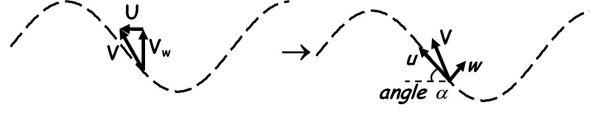


Figure 12. Lighthill [10] decomposed the resultant velocity V at a point on the surface into a component u tangential to it (causing resistive drag) and a component w normal to it (causing reactive thrust).

where α is the angle as shown in Fig. 12. Lighthill [11] then stated that the added mass due to the normal component w will be large and therefore it will primarily contribute to the so-called “reactive” force. The axial component of this reactive force was termed thrust. He stated that the tangential component u will have only small contribution to the added mass and thus it will contribute predominantly to the viscous resistance. The axial component of the viscous force was termed drag. In this way, Lighthill formulated the decomposition of the force on the fin into drag- and thrust-causing mechanisms in spite of nonlinearities at high Reynolds numbers. Note that the decomposition of the fin velocity into u and w does not satisfy the realizability condition D2. Lighthill developed expressions to obtain the reactive thrust due to w for elongated bodies or fins [11, 12]. Since thrust T was assumed to be caused by w , according to equation 8, it is a function of $U_w - U$ [12]. The thrust is directed in the forward direction, as desired, when $U_w - U > 0$, whereas it is directed backward when $U_w - U < 0$. According to Lighthill, drag must be a function of U_w and $(U_w - U)$ since it is caused by u (equation 9). However, no expressions for drag were developed.

As shown in Fig. 2 and Table 4, below, the decomposition proposed in this work is different from

	Lighthill	Current Study
Drag	$u = \frac{U_w}{\cos[\alpha]} - (U_w - U) \cos[\alpha]$	$u_s = \frac{U_w}{\cos[\alpha]}$
Thrust	$w = (U_w - U) \sin[\alpha]$	$w_f = (U_w - U) \sin[\alpha]$ $u_f = -(U_w - U) \cos[\alpha]$

Table 4. Comparison of Lighthill’s kinematic decomposition and the one proposed here.

Lighthill's. The velocities u_s and u_f that are tangential to the wave surface in our slithering and frozen fin modes, respectively, are given by

$$u_s = U_w / \cos[\alpha], \quad (10)$$

$$u_f = -(U_w - U) \cos[\alpha]. \quad (11)$$

The tangential velocity in the slithering mode according to equation 10 corresponds only to the first part of the tangential velocity u according to Lighthill's decomposition in equation 9. The tangential velocity in our frozen fin mode (equation 11) corresponds to the second part of the tangential velocity u in equation 9. The normal velocity in the slithering mode is zero whereas that in the frozen fin mode w_f is given by

$$w_f = (U_w - U) \sin[\alpha], \quad (12)$$

This normal velocity is the same as w in equation 8. Thus, our results suggest that part of the tangential velocity u in the decomposition of Lighthill [11] that depends on $(U_w - U)$ is in fact coupled with the normal component to account for the thrust force according to the frozen fin mode.

In our decomposition the drag force is a function of U_w unlike the consequence of Lighthill's decomposition where the drag force is expected to be a function of U_w and $(U_w - U)$. The thrust force in our case is a function of $(U_w - U)$ like Lighthill but it has an additional contribution from the tangential velocity along the fin surface.

B Optimal height of the ribbon fin: Analysis

B.1 Swimming velocity

In Fig. 6b we presented the swimming velocity obtained from self-propulsion simulations. In this section we will show that it can also be obtained based on a reduced order model. Doing so will provide insights into the mechanisms underlying the simulation data.

The steady swimming velocity of a self-propelling organism is the one at which the resultant force on the body, averaged over a swimming cycle, is zero. In case of the fin-plate assembly, forces on the plate and the fin are decoupled as seen in Fig. 13. Therefore, at steady swimming $F_f[U_w, U, h] - F_p[U] = 0$, where square brackets indicate "function-of" and U is the translational velocity of the plate-fin assembly.

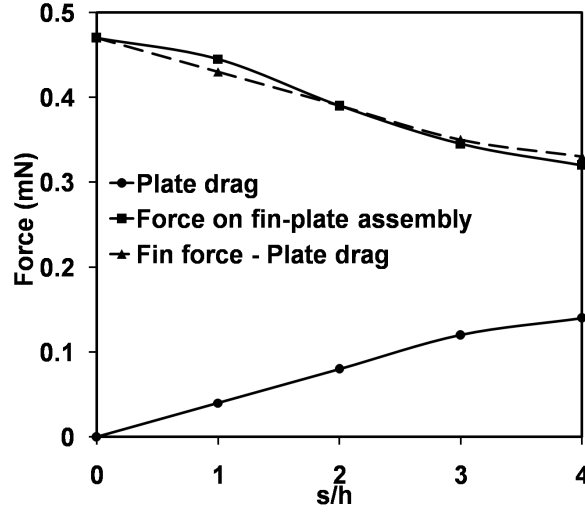


Figure 13. Force F_p on the plate (—●—), force F_{fp} on the fin-plate assembly (—■—), and $F_f - F_p$ (—▲—) as a function of s/h . Agreement between F_{fp} and $F_f - F_p$ shows that there is no momentum enhancement.

The value of U that satisfies the force equation is the swimming velocity U_s . Only U_w, U and h are the parameters of interest in this analysis. Remaining parameters are assumed to be constant.

According to the drag-thrust decomposition discussed in the Manuscript, $F_f = T_f - D_f$, where T_f and D_f are the thrust and drag forces on the ribbon fin, respectively. It was found that D_f depends on the wave velocity U_w whereas T_f depends on $(U_w - U)$. Using the drag-thrust decomposition of the force F_f on the fin, the force balance equation for the plate-fin assembly during steady swimming can be written as

$$T_f[U_w - U, h] - D_f[U_w, h] - F_p[U] = 0. \quad (13)$$

The functions for T_f , D_f , and F_p are obtained as follows. Fig. 3c shows that T_f depends on $(U_w - U)$. A combination of linear and quadratic variations fit the graph well. Since the mechanism of thrust generation is shown to be the low pressure caused by flow separation, thrust is proportional to the effective frontal area of the flapping ribbon fin which scales as h^2 . The drag force D_f is shown to be due to a boundary layer type flow caused by the slithering motion (Fig. 4). It depends on U_w (Fig. 3b), which is a constant in our simulations. The drag force is proportional to the wetted surface area of the ribbon fin which scales as h . Finally, F_p is caused primarily by the boundary layer on the plate. Hence, it is proportional to $U^{3/2}$ (all other parameters are constant). Thus, equation 13 can be written in the

following form

$$\{A_1(U_w - U)^2 + A_2(U_w - U)\}h^2 - Bh - CU^{3/2} = 0, \quad (14)$$

where A_1 , A_2 , B , and C are constants. The term involving h^2 is the thrust force T_f , $D_f = Bh$, and $F_p = CU^{3/2}$. Note that $U_w = 15$ cm/s for all cases considered here. Based on the data in Figures 3b and 3c, we find that $A_1 = 0.0059$ mN-s²/cm⁴, $A_2 = 0.0068$ mN-s/cm³, and $B = 0.51$ mN/cm. We did simulations for flow over a plate and found that $C = 0.017$ mN/(cm/s)^{3/2}. The only unknowns in equation 14 are U and h . Thus, it can be used to obtain the swimming velocity U_s as a function of h .

Analytic solution for U_s : Now we solve the analytic equation 14 and compare it to the swimming velocity computed from self-propulsion simulations of the fin-plate assembly (Fig. 6b). It is possible to obtain an approximate closed form solution for h as a function of U_s by solving equation 14. To do so we note that equation 14 is a quadratic equation for h . Using the quadratic formula for h , keeping the physically relevant solution, and using binomial expansion of a square-root term up to first order, we get the following solution

$$h = \frac{B}{A_1(U_w - U_s)^2 + A_2(U_w - U_s)} + \frac{CU_s^{3/2}}{B}. \quad (15)$$

The first part on the right hand side corresponds to the swimming of an isolated fin and the second part is the correction due to the drag on the plate. The above equation is solved for U_s and is compared to the values computed from self-propulsion simulations in Fig. 6b. Also plotted in Fig. 6b is the analytic solution for a hypothetical freely swimming ribbon fin without a plate attached. That solution is obtained from equation 15 by substituting $C = 0$. Below a critical height h_c the analytic swimming velocity becomes negative. Analytic solution in this regime is not plotted since the drag-thrust split model is not valid in this regime. There is no self-propulsion simulation data in this regime since the swimming velocity is very small and the numerical accuracy is not sufficient. The trends in Fig. 6b will be discussed below in two parts: **1)** trends for swimming velocity above the critical fin height, and **2)** swimming at fin heights below the critical value.

1) Fig. 6b shows that, for fin heights above a critical value, the swimming velocity from self-propulsion simulations is in good agreement with the analytic curve for a plate-fin assembly at smaller h and agrees better with the analytic curve for the fin-only case at larger h . This is expected because at h comparable to or larger than the plate height of $s = 2$ cm, the plate drag is dominated by the drag of the ribbon fin. Hence, the plate-fin assembly swims at a velocity that is close to the self-propulsion velocity of the

ribbon fin itself. The disagreement between simulated and analytic swimming velocities of the plate-fin assembly, at larger h , arises because the higher-order terms in the binomial expansion were neglected in equation 15.

The key trend of U_s is the rapid rise with respect to h at smaller h and a slow change at larger h . This variation is the primary factor that determines the cost of transport (COT) trends obtained in Fig. 6c. It is clear from Figure 6b that the trend in U_s is inherent to the self-propulsion velocity of the isolated ribbon fin itself. The presence of the plate drag merely plays a role in shifting the swimming velocity to a lower value. Equations 14 and 15 imply that the root cause of the trend in U_s is the fact that the fin thrust T_f scales as h^2 while the fin drag D_f scales as h , and the fact that the swimming velocity affects only T_f . Due to this, at smaller h , any increase in fin height increases the drag more than the thrust. To achieve a balance between drag and thrust, the swimming velocity must increase significantly so that the thrust is large enough to equal the drag. For larger h the effect is opposite. Any increase in h causes larger increase in thrust compared to drag. Hence, to achieve drag-thrust balance the swimming velocity needs to change only slightly.

2) The analytic solution leads to a critical height h_c at which the swimming velocity is zero (Figure 6b). The analytic solution is not valid for this and smaller heights because the drag-thrust split model for the fin force is not accurate. The swimming velocities at fin heights below the critical value, computed from self-propulsion simulations, are very small indicating inefficient swimming, i.e., large COT. Thus, optimal swimming conditions do not fall within this regime. We do not present these data because the numerical accuracy was not sufficient to report them quantitatively. It was computationally expensive for us to explore this regime because very refined meshes are required in this case to resolve the flow due to a tiny ribbon fin attached to a large plate.

B.2 Cost of transport (COT)

To understand the COT trends we first consider the trend of average power plotted in Fig. 6a. It is seen that the data fit a single curve that scales as h^3 over the entire range. It is found from our computations that the power is dominated by the work done to flap the ribbon fin laterally. The velocity V_w of lateral motion is maximum at the bottom edge of the ribbon fin and scales as $h\theta_{\max}f$. Thus, the power is expected to scale as $\rho V_w^3 A$, where A is some scale for area. The power spent is not substantially influenced by the swimming velocity for the scenarios considered here. Our computations also show that

the dominant contribution to power spent from lateral flapping comes from the bottom edge of the fin. Thus, the appropriate scale for A is not expected to depend strongly on h . Therefore, it follows that power $P \sim h^3$, consistent with Figure 6a.

To compute the COT analytically we use the curve fit for power in Fig. 6a and divide it by the analytically obtained swimming velocity (equation 15). This is plotted in Fig. 6c and compared with the COT computed from self-propulsion simulations. The agreement is found to be good.

The analytic solution helps to better understand the trend in $\text{COT} = P/U_s$ above the critical fin height. Since the swimming velocity changes faster with respect to h at lower values of h , it compensates for the h^3 rise of power. This gives the low and nearly constant trend of COT with respect to h in the simulation data. At larger h the swimming velocity increases with respect to h at a rate that is less than h^3 . Hence, $\text{COT} = P/U_s$ increases with respect to h , thus, making swimming with a larger fin less and less effective. As noted before, the variation in the swimming velocity can be understood in terms of different scalings, with respect to h , of the drag and thrust of the ribbon fin. Therefore, the key factors that explain the trends in COT with respect to the fin height are the different mechanisms of drag and thrust on the ribbon fin.

B.3 Effect of a realistic fish body drag

In case of the idealized plate-fin swimmer, the plate drag is dominated by boundary layer flow and scales as $U^{3/2}$. In case of an actual fish, this may not be an accurate drag estimate due to the presence of form drag on the body. To ensure that the key features obtained in the idealized plate-fin model are not affected by this factor, we consider an analytic solution with a different body drag. To that end, we replace the plate drag term $CU^{3/2}$ in equation 14 with EU^2 , which represents the typical pressure drag scaling at high Reynolds numbers. Our prior simulations for the drag force on a realistic CAD model of the body of a black ghost knifefish [30], give $E = 0.055 \text{ mN}\cdot\text{s}^2/\text{cm}^2$. Using this drag model for the body we find the analytic solution for the swimming velocity. Then we estimate the COT for the body-fin assembly by assuming that the primary contribution to power comes from the fin – which was verified in the plate-fin case. To obtain COT, we use the same power curve as that in Fig. 6a and divide it by the analytically calculated swimming velocity based on the body drag model. Fig. 6c shows a comparison between the COT for the plate-fin and body-fin assemblies. The key features pertaining to the minimum in COT are the same. Thus, all the trends discussed above about optimal fin height are applicable even

with a realistic body drag.

C Sensitivity of COT to perturbations in plate height

We measured the body and the fin height of 13 species from 8 genera of South American weakly electric fishes in the family Aptereronotidae (see Section 4.3 and Table 3). We found that the mean body height, at mid-fin length, was 1.86 cm with a standard deviation of 0.85 cm. The mean fin height, at mid-fin length, was measured to be 0.97 cm. This is within the range our prediction for optimal fin height. Although the standard deviation of the fin height is as high as 0.84 cm, the measured fin height does not vary significantly. The standard deviation of fin height is 0.33 cm.

In this section we investigate how sensitive the COT trend is to variations in plate height. Note that the COT trend is the one that leads to the prediction of the fin height. For this, holding the fin height constant, we first find the rate of change of swimming speed with plate height using equation 15. The rate of change of velocity is then used to find the change in cost of transport due to perturbations in plate height. The change in cost of transport will provide insights into how optimal fin height will change with plate height.

The rate of change of swimming velocity with plate height, after differentiating equation 15 at constant fin height, is given by

$$\frac{\partial U_s}{\partial s} = -\frac{C'U^{3/2}}{B} \left[\frac{B(2A_1(U_w - U_s) + A_2)}{(A_1(U_w - U_s)^2 + A_2(U_w - U_s))^2} + \frac{3C\sqrt{U_s}}{2B} \right], \quad (16)$$

where $C' = \partial C / \partial s$. The drag on the plate has a linear dependence on the plate height. Consequently, C will also have a linear dependence on plate height. We find $C' = \partial C / \partial s = 0.0085 \text{ mN}\cdot\text{s}^{3/2}/\text{cm}^{3/2}$.

The rate of change of cost of transport is found by taking the derivative of P/U_s with respect to s at constant fin height. It is given by

$$\frac{\partial COT}{\partial s} = -\frac{COT}{U_s} \frac{\partial U_s}{\partial s}. \quad (17)$$

The change in cost of transport, ΔCOT , due to a perturbation in plate height, Δs , is computed using the above equation. This is used to estimate the change in the computed value of the cost of transport corresponding to the standard deviation of the measured body height of fishes. These estimated changes

are plotted in Figure 6. It is seen that although the plate height does vary, the corresponding variation in COT is very small at small fin height h , while at larger values of h the change is moderate. In short, the basic trend of the COT with fin height is unaltered by changes to the plate height.

D Navier-Stokes equation

The Navier-Stokes equation for incompressible flow

$$\frac{\partial \mathbf{u}}{\partial t} + (\mathbf{u} \cdot \nabla) \mathbf{u} = -\frac{1}{\rho} \nabla p + \nu \nabla^2 \mathbf{u}, \quad (18)$$

where \mathbf{u} is the fluid velocity, p is the pressure, ν is the kinematic viscosity of the fluid, and ρ is the fluid density. The second term on the left-hand-side is the nonlinear inertia term referred to in the Manuscript.

References

1. Grillner, S., 2003 The motor infrastructure: from ion channels to neuronal networks. *Nature Reviews Neuroscience* **4**, 573–586.
2. McLean, D. L., Masino, M. A., Koh, I. Y., Lindquist, W. B. & Fetcho, J. R., 2008 Continuous shifts in the active set of spinal interneurons during changes in locomotor speed. *Nature neuroscience* **11**, 1419–1429.
3. Turner, R. W., Maler, L. & Burrows, M., 1999 Special issue on electroreception and electrocommunication. *J. Exp. Biol.* **202**, 1167–1458.
4. Krahe, R. & Fortune, E., 2013 Electric fishes: neural systems, behavior and evolution. *J. Exp. Biol.* .
5. MacIver, M. A., Fontaine, E. & Burdick, J. W., 2004 Designing future underwater vehicles: principles and mechanisms of the weakly electric fish. *IEEE J. Ocean. Eng.* **29**, 651–659.
6. Neveln, I. D., Bai, Y., Snyder, J. B., Solberg, J. R., Curet, O. M., Lynch, K. M. & MacIver, M. A., 2013 Biomimetic and bio-inspired robotics in electric fish research. *Journal of Experimental Biology* **216**, in press.
7. Colgate, J. E. & Lynch, K. M., 2004 Mechanics and control of swimming: A review. *IEEE Journal of Oceanic Engineering* **29**, 660–673.
8. Webb, P. W., 1984 Form and function in fish swimming. *Sci. Am.* **251**, 58–68.
9. Ruiz-Torres, R., Curet, O. M., Lauder, G. V. & MacIver, M. A., 2013 Kinematics of the ribbon fin in hovering and swimming of the electric ghost knifefish. *The Journal of Experimental Biology* **216**, 823–834.
10. Lighthill, J., 1975 *Mathematical biofluidynamics*. Philadelphia, PA: SIAM.
11. Lighthill, J., 1971 Large-amplitude elongated-body theory of fish locomotion. *Proc. Roy. Soc. B.* **179**, 125–138.
12. Lighthill, J. & Blake, R., 1990 Biofluidynamics of balistiform and gymnotiform locomotion 1. Biological background, and analysis by elongated-body theory. *J. Fluid Mech.* **212**, 183–207.

13. Blake, R. W., 1983 Swimming in the electric eels and knifefishes. *Can. J. Zool.* **61**, 1432–1441.
14. Shirgaonkar, A. A., Curet, O. M., Patankar, N. A. & MacIver, M. A., 2008 The hydrodynamics of ribbon-fin propulsion during impulsive motion. *J. Exp. Biol.* **211**, 3490–3503.
15. Neveln, I. D., Bale, R., Bhalla, A. P. S., Curet, O. M., Patankar, N. A. & MacIver, M. A., 2013 Undulating fins produce off-axis thrust and flow structures. *Journal of Experimental Biology* p. in press.
16. Videler, J. J. & Hess, F., 1984 Fast continuous swimming of two pelagic predators, saithe (*pollachius virens*) and mackerel (*scomber scombrus*): A kinematic analysis. *J. Exp. Biol.* **109**, 209–228.
17. Tytell, E. D. & Lauder, G. V., 2004 The hydrodynamics of eel swimming: I. Wake structure. *J. Exp. Biol.* **207**, 1825–1841.
18. Borazjani, I. & Sotiropoulos, F., 2008 Numerical investigation of the hydrodynamics of carangiform swimming in the transitional and inertial flow regimes. *Journal of Experimental Biology* **211**, 1541–1558.
19. MacIver, M. A., Sharabash, N. M. & Nelson, M. E., 2001 Prey-capture behavior in gymnotid electric fish: Motion analysis and effects of water conductivity. *J. Exp. Biol.* **204**, 543–557.
20. Shirgaonkar, A. A., MacIver, M. A. & Patankar, N. A., 2009 A new mathematical formulation and fast algorithm for fully resolved simulation of self-propulsion. *J. Comput. Phys.* **228**, 2366–2390.
21. Peng, J. & Dabiri, J., 2008 The ‘upstream wake’ of swimming and flying animals and its correlation with propulsive efficiency. *The Journal of Experimental Biology* **211**, 2669–2677.
22. Fish, F. E. & Lauder, G. V., 2006 Passive and active flow control by swimming fishes and mammals. *Ann. Rev. Fluid Mech.* **38**, 193–224.
23. Schultz, W. W. & Webb, P. W., 2002 Power requirements of swimming: Do new methods resolve old questions? *Integr. Comp. Biol.* **42**, 1018–1025.
24. Shen, L., Zhang, X., Yue, D. K. P. & Triantafyllou, M. S., 2003 Turbulent flow over a flexible wall undergoing a streamwise travelling wave motion. *J. Fluid Mech.* **484**, 197–221.

25. Albert, J. S., 2001 Species diversity and phylogenetic systematics of american knifefishes (gymnotiformes, teleostei). *Misc. Publ. Mus. Zool. Univ. Mich.* **190**, 1–127.
26. Curet, O. M., Patankar, N. A., Lauder, G. V. & MacIver, M. A., 2011 Mechanical properties of a bio-inspired robotic knifefish with an undulatory propulsor. *Bioinspir. Biomim.* **6**.
27. Kern, S. & Koumoutsakos, P., 2006 Simulations of optimized anguilliform swimming. *J. Exp. Biol.* **209**, 4841–4857.
28. Albert, J. S. & Crampton, W. G. R., 2005 Diversity and phylogeny of neotropical electric fishes (Gymnotiformes). In *Electroreception*, pp. 360–409. New York: Springer.
29. Crampton, W. G. R. & Albert, J. S., 2006 Evolution of electric signal diversity in gymnotiform fishes. In *Communication in Fishes* (eds. F. Ladich, S. Collin, P. Moller & B. Kapoor), pp. 641–725. Science Publishers Inc., Enfield, NH.
30. MacIver, M. A., Shirgaonkar, A. A. & Patankar, N. A., 2010 Energy-information trade-offs between movement and sensing. *PLoS Comput. Biol.* **6**, e1000769.